metals

MDPI

Article

Effect of CaO Content and Annealing Treatment on the Room-Temperature Mechanical Properties of AZ61 and AZ61-CaO Alloys

Umer Masood Chaudry [1,2,†], Hafiz Muhammad Rehan Tariq [1,†], Nooruddin Ansari [3], Adil Mansoor [4], Muhammad Kashif Khan [5,6,*], Kotiba Hamad [7,*] and Tea-Sung Jun [1,2,*]

1 Department of Mechanical Engineering, Incheon National University, Incheon 22012, Republic of Korea; umer@inu.ac.kr (U.M.C.)
2 Research Institute for Engineering and Technology, Incheon National University, Incheon 22012, Republic of Korea
3 Department of Materials Science & Engineering, Chungnam National University, Daejeon 34134, Republic of Korea
4 College of Physics and Optoelectronics Engineering, Shenzhen University, Shenzhen 518060, China
5 School of Chemical Engineering, Sungkyunkwan University, Suwon 16419, Republic of Korea
6 School of Mechanical Engineering, Sungkyunkwan University, Suwon 16419, Republic of Korea
7 School of Advanced Materials Science & Engineering, Sungkyunkwan University, Suwon 16419, Republic of Korea
* Correspondence: kashifkhan@skku.edu (M.K.K.); hamad82@skku.edu (K.H.); t.jun@inu.ac.kr (T.-S.J.)
† These authors contributed equally to this work.

Abstract: In the present study, the effect of annealing treatment on the room-temperature mechanical performance of AZ61, AZ61-0.5CaO and AZ61-1CaO was thoroughly investigated. The as-rolled samples were annealed at 400 °C for 1 h followed by furnace cooling. Microstructural characterization was carried out using optical microscopy (OM), scanning electron microscopy (SEM), transmission electron microscopy (TEM) and electron back-scattered diffraction (EBSD). Moreover, room-temperature uniaxial tensile tests were carried out on the non-annealed and annealed samples along the rolling direction at the strain rate of 10^{-3} s^{-1}. Microstructural analysis showed the presence of profuse $\{10\bar{1}2\}$ twinning in non-annealed samples and the twinning fraction was increased by the addition of CaO content. SEM showed the formation of precipitates in the AZ61-CaO alloys and TEM confirmed the precipitates to be $(Mg, Al)_2Ca$. The room-temperature tensile tests showed that the mechanical properties of AZ61 were slightly reduced by the addition of CaO, which was attributed to the higher local stress concentration due to the twin–twin interactions. Furthermore, the annealing treatment led to significant enhancement in the YS and UTS of AZ61-1CaO, which is related to the precipitation hardening induced by the intermetallic precipitates.

Keywords: magnesium; strength; texture; AZ61; Mg-CaO alloys; heat treatments; EBSD

check for updates

Citation: Chaudry, U.M.; Tariq, H.M.R.; Ansari, N.; Mansoor, A.; Khan, M.K.; Hamad, K.; Jun, T.-S. Effect of CaO Content and Annealing Treatment on the Room-Temperature Mechanical Properties of AZ61 and AZ61-CaO Alloys. *Metals* **2023**, *13*, 1962. https://doi.org/10.3390/met13121962

Academic Editor: Talal Al-Samman

Received: 10 November 2023
Revised: 29 November 2023
Accepted: 30 November 2023
Published: 1 December 2023

Copyright: © 2023 by the authors. Licensee MDPI, Basel, Switzerland. This article is an open access article distributed under the terms and conditions of the Creative Commons Attribution (CC BY) license (https://creativecommons.org/licenses/by/4.0/).

1. Introduction

Global warming due to the increasing CO_2 emissions produced by the automobile industry upsets the planet's energy balance, resulting in rising temperatures and associated climatic changes. Magnesium (Mg) alloys can play a vital role in combating global warming through their lightweight properties, contributing to reduced emissions in transportation and manufacturing. Enhanced energy efficiency in industrial processes further supports environmental sustainability efforts. Mg alloys are advantageous in terms of their high specific strength with low density and good recyclability [1–6]. However, the conventional hot metal forming process on a hexagonal close-packed structured (HCP) Mg alloy results in the development of a dominant (0001) strong basal texture, leading to premature plastic deformation at ambient temperatures [7–19]. This limits the usage of Mg alloys in structural

applications. It is well known that strategic alloying for Mg with rare earth elements (REs) restricts the favorable basal orientation of the crystal and produces more random orientations within the crystal structure, hence leading to the better ductility and formability of the alloy [20–29].

Among other Mg alloys, Mg-Al-Zn alloys are very commonly used worldwide due to their higher strength. The presence of α-Mg and β-$Mg_{17}Al_{12}$ phase distributions in the matrix strengthens the alloy but at the same time can cause early fractures [30–38]. This problem can be addressed with the alloying additions of RE elements which reduce Al and form Al-RE compounds instead of the brittle $Mg_{17}Al_{12}$ compounds [39–43], but due to the high costs and reduced availability of RE, its use is constrained for large-scale production. Therefore, other elements, such as calcium, are added, thereby creating thermally stable intermetallic particles with Al (Al_2Ca) and limiting the formation of the thermally unstable $Mg_{17}Al_{12}$ phase. It has previously been shown that the addition of Ca in AZ31 Mg alloy softened prismatic slips and the difference between $CRSS_{basal}$ and $CRSS_{prismatic}$ decreased considerably [34,44–50]. Although Ca is relatively more cost-effective than RE elements, it is crucial to consider that both the extraction of elemental Ca and the integration of Mg-Ca master alloy can increase production costs. Recently, CaO has gained a lot of attention from scientists due to its stability and cost-effectiveness, and has replaced Ca as an alloying addition for modifying the Mg-AZ alloy series. According to Zhao et al., the addition of CaO in AZ91 Mg alloy led to the uniform distribution of second-phase particles at the grain boundaries of α-Mg and refined the grain size, resulting in the alloy demonstrating better mechanical properties [51]. Additionally, MgO is more stable than CaO at low temperatures, and thus the reduction in CaO that occurs during the melt-mixing process leads to the homogenous distribution of Ca in the Mg matrix. For instance, TW Lee et al. reported a significant increase in the volume fraction of Al_2Ca second-phase particles with uniform distribution in AZ31 Mg alloy when CaO was introduced as an alloying addition [52].

Annealing is an important heat treatment process to influence the deformation behavior of a material. This can eradicate the localized stresses, anneal the microstructure and improve the precipitation strengthening mechanism. For example, Liu et al. proposed that double-stage annealing of Mg-6Zn-3Sn gave rise to the formation of a Zn and Sn solid solution and the uniform distribution of Mg_2Sn precipitates, which improved the mechanical properties of the materials [53]. Furthermore, Rehan et al. reported a twin free coarse grain microstructure in AZ61 Mg alloy after annealing in a recent study [54]. Annealing treatment after the initial metal-forming process of AZ-Mg alloy with secondary phases can accelerate the particle-stimulated nucleation (PSN) mechanism, which further promotes recrystallization and inhibits the favorable basal orientation of the crystals, hence leading to a more randomized texture in the alloy.

Until now, studies of AZ61 Mg alloy with different concentrations of CaO alloying additions along with annealing treatment are relatively rare. Therefore, it is necessary to study the annealing effect combined with CaO alloying on AZ61 Mg alloy in detail. For this reason, the present study investigated AZ61, AZ61-0.5CaO and AZ61-1CaO deformation behavior before and after annealing treatment. Also, the microstructure and texture evolution during annealing treatment of these alloys were studied in detail.

2. Materials and Methods

In this study, hot-rolled plates of AZ61, AZ61-0.5CaO and AZ61-1CaO (wt.%) alloys were employed. These alloys were produced by casting commercial AZ61 magnesium alloy and CaO powder, and cast billets with a thickness of 30 mm were fabricated. The casted billets were preheated to 350 °C for 1 h and underwent multi-pass hot rolling until a thickness of 1 mm was achieved. Samples were then annealed at 400 °C for 1 h. For microstructural and textural characterization, coupons were extracted from the RD-TD (rolling direction–transverse direction) plane of each sample and prepared as per standard metallographic procedures [43]. The prepared samples were examined under a Carl Zeiss optical microscope. Additionally, a scanning electron microscope (SEM, SU-5000, Hitachi,

Tokyo, Japan) and energy dispersive spectroscopy (EDS, JSM-7800F, JEOL, Tokyo, Japan) were utilized to determine the elemental composition and identify intermetallic particles dispersed throughout the microstructure. For a more detailed analysis of the segregation and elemental composition of particles within AZ61-1CaO, a field emission transmission electron microscope (FE-TEM/STEM-EDS, Thermo Fisher Scientific Talos F200X, Waltham, MA, USA) was employed. The crystallographic orientation of the samples was determined using SEM equipped with an electron back-scattered diffraction analysis system (EBSD, VelocityTM Super, EDAX, Mahwah, NJ, USA). A scanning area of 100 × 250 μm^2 and a step size of 0.1 μm were used for all samples. The microstructural and crystallographic orientation data obtained from EBSD were processed using TSL OIM version 8.6. The mechanical properties of both the annealed and non-annealed alloys were assessed through uniaxial tensile tests conducted at room temperature (RT). Dog-bone-shaped tensile samples of AZ61, AZ61-0.5CaO and AZ61-1CaO alloys, each with a gauge length of 25 mm, width of 6 mm and thickness of 1 mm, were tested using a universal testing machine (UTM, RB 301 UNITECH-T, R&B, Singapore) along the rolling direction. An extensometer (Axial Extensometers, 3542, Epsilon Tech., Jackson, WY, USA) was used to measure the elongation during deformation. All tests were conducted and repeated thrice to ensure reproducibility.

3. Results and Discussion

Figure 1 illustrates the initial optical micrograph (OM) of the annealed and non-annealed samples of AZ61 alloys with varying CaO contents. The OM images of non-annealed samples presented in Figure 1a–c reveal that all the alloys exhibited a partially recrystallized microstructure with the presence of profuse twinning, which can be attributed to the primary rolling process. Moreover, the twinning fraction was observed to increase with the addition of CaO. The OM maps of annealed samples of AZ61, AZ61-0.5CaO and AZ61-1CaO are displayed in Figure 1d,e, respectively. Two major differences can be readily observed. Firstly, the annealing led to a significant reduction in the twinning fraction and only a few twinned grains can be noticed. Secondly, the evolution of a fully recrystallized microstructure consisting of coarse grains in addition to small clusters of fine grains was detected. The emergence of recrystallized grains after the annealing treatment can be anticipated to be governed by the particle-stimulated nucleation (PSN) effect due to the dispersed secondary phase particles. To confirm the type and morphology of precipitates, SEM and TEM-EDS analysis was carried out.

Figure 2a–c show the SEM images with EDS spectra entailing the area and point analysis of AZ61, AZ61-0.5CaO and AZ61-1CaO, respectively. It can be seen that AZ61-0.5CaO contains large-sized Mg-Al-Ca compounds within the Mg matrix. Here, the formation of Mg-Al-Ca compounds can be attributed to the low solubility of calcium within the Mg matrix. The increase in CaO content from 0.5% to 1% led to higher formation of Al_2Ca compounds. This is because the higher concentration of Ca likely exceeds the threshold required to form stable Mg-Ca-rich compounds. Further TEM/EDS analysis of AZ61-1CaO (Figure 2d) confirms the formation of Al_2Ca compounds distributed in the Mg matrix. It is noteworthy that the formation of common brittle phase ($Mg_{17}Al_{12}$) in Al-Zn Mg alloys is repressed significantly because of Al consumption in forming Al_2Ca or $(Mg, Al)_2Ca$ phases, which is consistent with previous studies [34,35,55–57]. In addition, it was in accordance with the XRD patterns of AZ61, AZ61-0.5CaO and AZ61-1CaO as shown in Figure 2e, where new peaks related to $(Mg, Al)_2Ca$ can be seen.

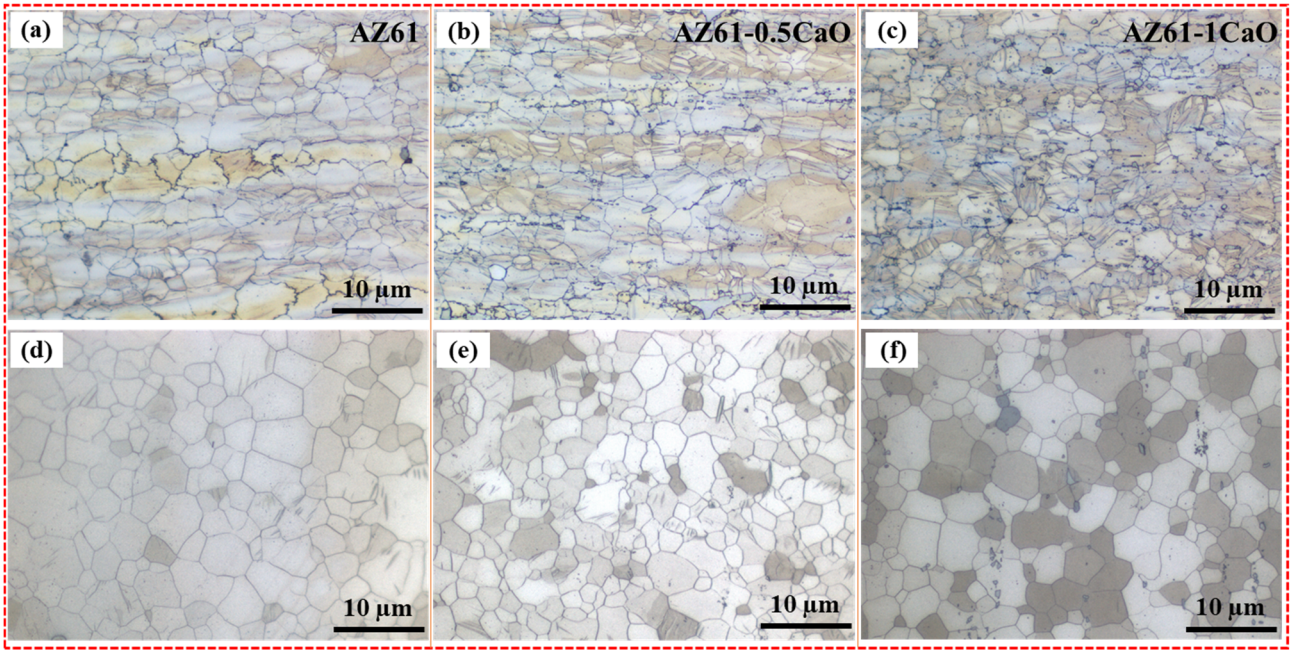


Figure 1. OM images of non-annealed and annealed samples of (**a**,**d**) AZ61, (**b**,**e**) AZ61-0.5CaO and (**c**,**f**) AZ61-1CaO.

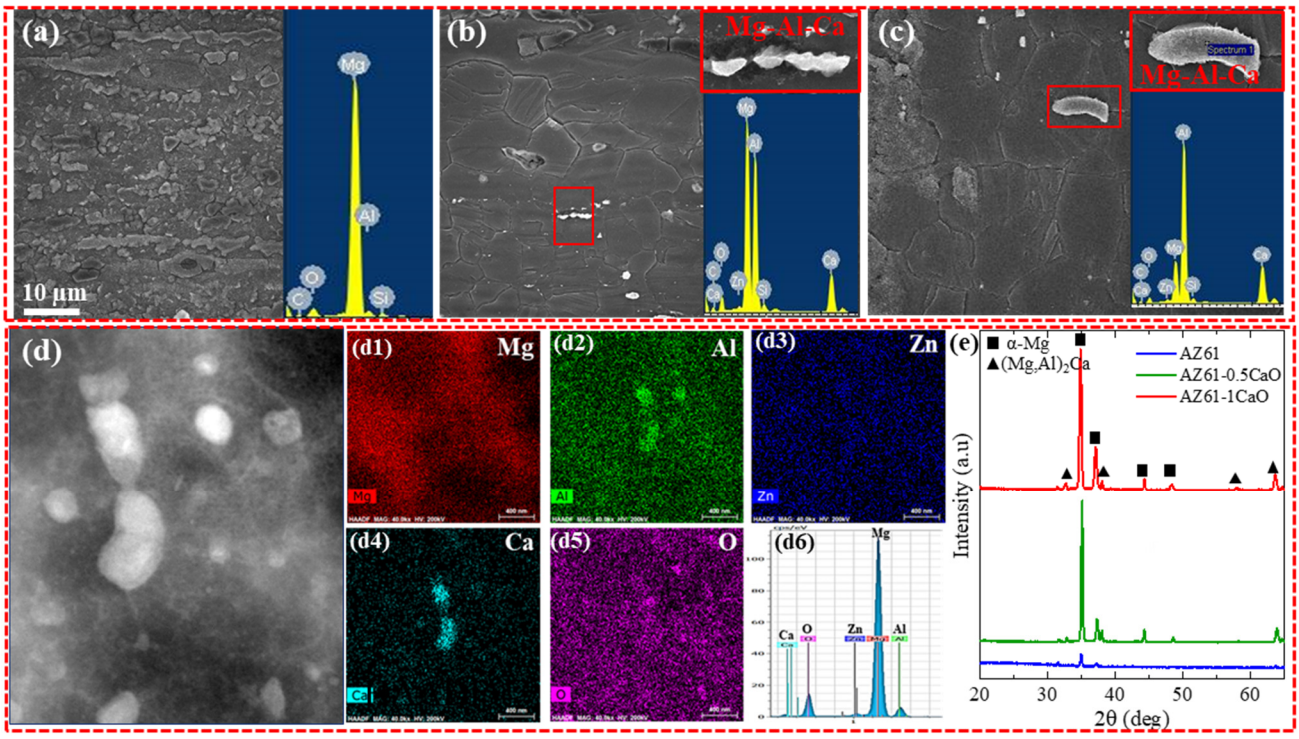


Figure 2. SEM images and point EDS analysis of as-received (**a**) AZ61, (**b**) AZ61-0.5Ca and (**c**) AZ61-1CaO. (**d**) Dark field TEM images of AZ61-1CaO and TEM-EDS elemental mapping; (**d1**–**d6**,**e**) X-ray diffraction patterns of AZ61, AZ61-0.5CaO and AZ61-1CaO.

Figure 3 depicts the EBSD IPF maps, KAM maps, basal pole figures and inverse pole figures of AZ61 alloys with varying CaO contents in their as-rolled (AR) state. The EBSD IPF maps presented in Figure 3a,d,e revealed that all the alloys exhibit a partially recrystallized microstructure and twins resulting from the hot rolling process. Notably, the addition of CaO has led to significant variations in misorientations, texture, grain sizes

and twinning fractions of AZ61 alloys. The KAM maps shown in Figure 3b illustrate that the average KAM value for as-rolled AZ61 alloys is 0.69. This value slightly increases to 0.72 for AZ61-0.5CaO (Figure 3e), and then decreases to 0.62 for AZ61-1CaO (Figure 3h). Consequently, the addition of CaO results in lower KAM values for the as-rolled samples. This can primarily be attributed to the reduced lattice distortion and increased dynamic recrystallization of AZ61-1CaO, leading to finer, strain-free grains. Additionally, the basal pole figures and inverse pole figures presented in Figure 3c indicate that AZ61 alloys exhibit mainly basal textures, which is a common rolling texture observed in Mg alloys. However, the addition of CaO has led to the development of non-basal texture components in AZ61-0.5CaO and AZ61-1CaO alloys as presented in Figure 3f,i. In particular, AZ61-1CaO alloys display a strong intensity near the non-basal poles, indicating the formation of non-basal grains, as also evident in the IPF map (Figure 3i). The evolution of non-basal texture components in CaO-containing alloys is mainly due to higher twinning ability, which rotates the grains away from basal orientations.

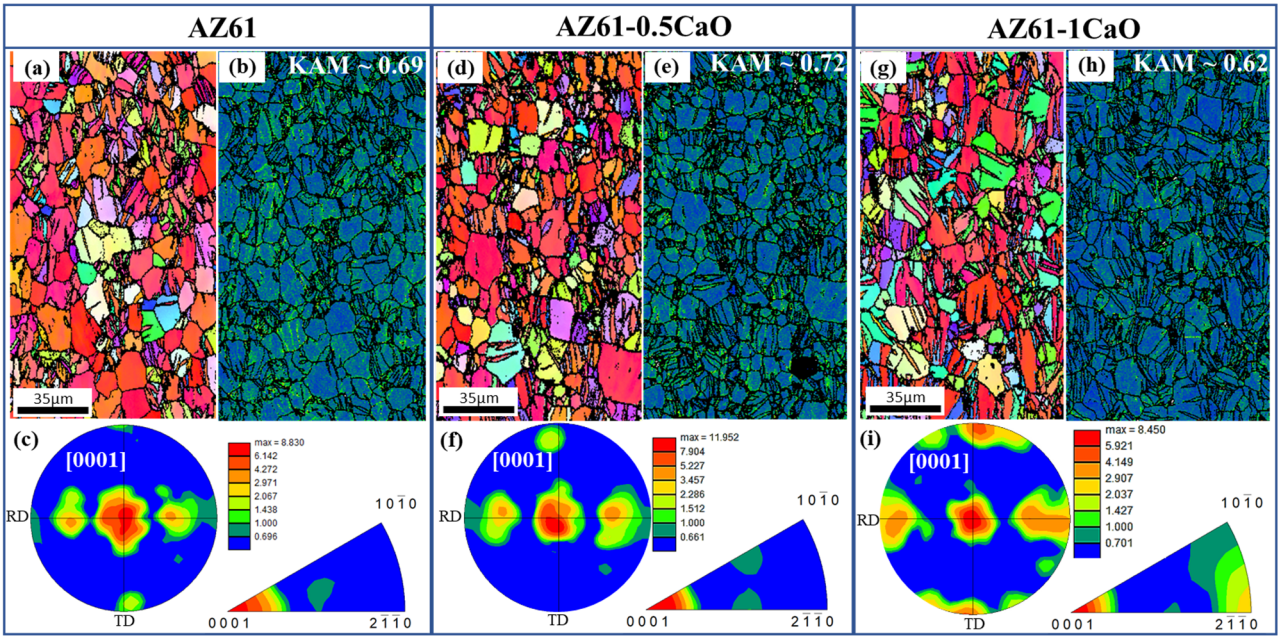


Figure 3. EBSD analysis including the (**a**,**d**,**g**) inverse pole figure map, (**b**,**e**,**h**) Kernel average misorientation map and (**c**,**f**,**i**) (0001) pole figure for non-annealed AZ61, AZ61-0.5Ca and AZ61-1CaO, respectively.

Figure 4 presents the grain size distribution and misorientation angle distribution of the AZ61, AZ61-0.5CaO and AZ61-1CaO alloys following the hot rolling process. Grain sizes were determined using the mean circle equivalent diameter method based on the EBSD data. The grain size distribution of the AZ61 alloy ranges from 0.98 µm to 19 µm, with an average grain size of 2.55 µm, as presented in Figure 4a. In comparison, for the AZ61-0.5 CaO alloy, the range narrows to 0.94 µm to 16.5 µm, with an average grain size of 2.32 µm (Figure 4b). Further reduction in grain size range is observed for AZ61-1CaO from 0.9 to 14.6 µm, with an average grain size of 2.28 µm, as illustrated in Figure 4c. Overall, the addition of CaO to AZ61 alloys leads to a decrease in average grain size with a minimal standard deviation. The AZ61-0.5CaO and AZ61-1CaO alloys contain Ca-rich second-phase particles, acting as nucleation sites for DRX during the hot-rolling process, ultimately resulting in finer grain sizes.

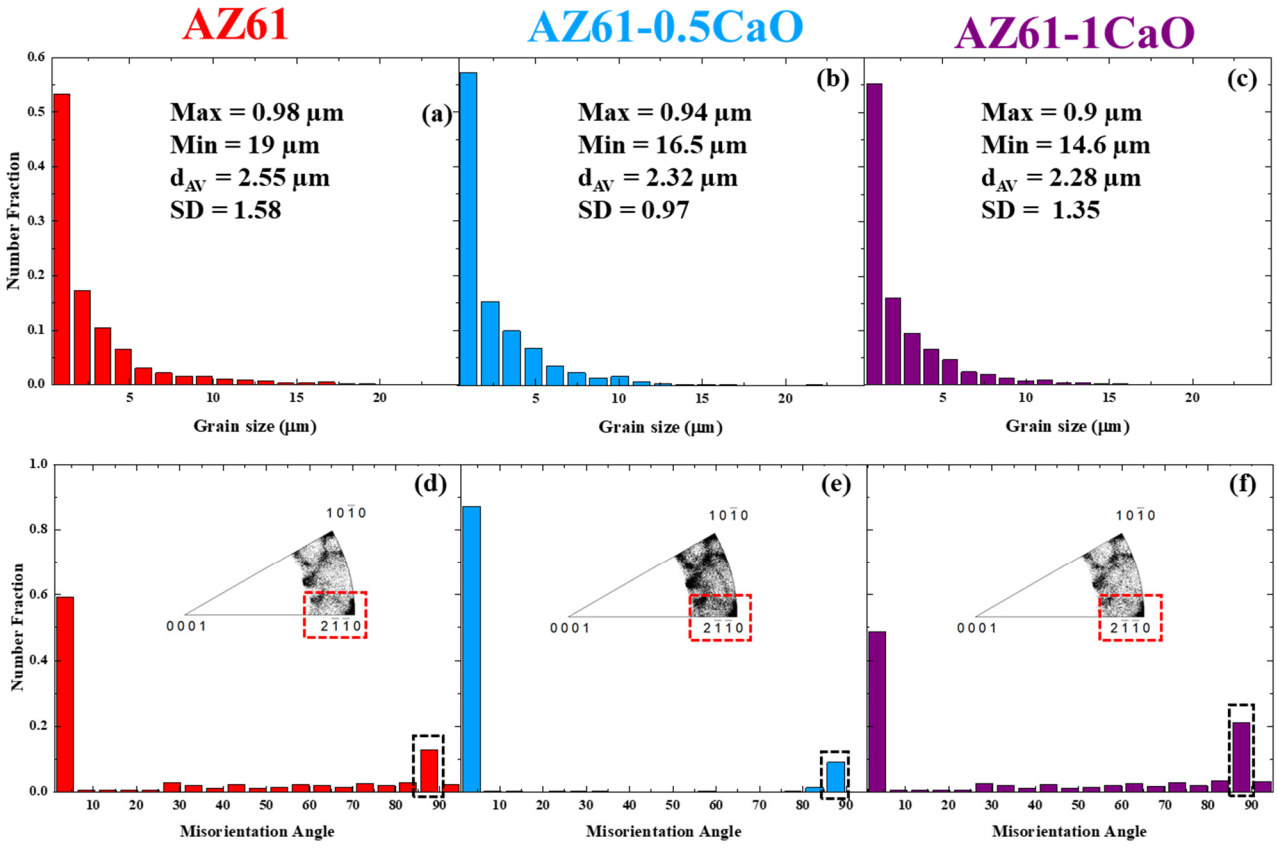


Figure 4. Grain size distribution and misorientation angle distribution of the non-annealed AZ61 (**a**,**d**), AZ61-0.5Ca (**b**,**e**) and AZ61-1CaO (**c**,**f**).

Moreover, the misorientation angle distribution displayed in Figure 4d–f indicates that the addition of CaO reduced the fraction of low-angle grain boundaries overall (LAGBs with misorientation less than 15°), whereas it increased the fraction of high-angle grain boundaries (HAGBs with misorientation greater than 15°) for AZ61-1CaO alloys. This increase in the fraction of HAGBs for AZ61-1CaO alloys can be attributed to the finer grain size and enhanced twinning ability of the alloy. As highlighted by the box, boundaries with misorientations close to 86.5° exhibit significant fractions, denoting the tension twins (TT) $\{2\bar{1}\bar{1}0\}$. This was also confirmed by the inset misorientation distribution function maps, which also show higher intensity near $\{2\bar{1}\bar{1}0\}$. Notably, the AZ61-1CaO alloy displays the highest fraction of boundary misorientation near 86.5°, indicating the highest tensile twin fractions (Figure 4f). This finding is consistent with the observation in the EBSD IPF map of the AZ61-1CaO alloy. This also suggests that the addition of CaO to AZ61 alloys reduces the critical stress required for the nucleation of TT.

To anneal the microstructure, the as-rolled samples underwent heat treatment at 400 °C for 1 h. Figure 5 shows the EBSD IPF maps, KAM maps and basal pole figures of the heat-treated AZ61, AZ61-0.5CaO and AZ61-1CaO alloys. Following heat treatment, the IPF maps for all the alloys reveal a fully recrystallized microstructure characterized by equiaxed grains and an absence of twins (Figure 5a,d,g). Notably, there are substantial disparities in misorientation, grain sizes and grain orientations among the alloys. The IPF map of AZ61 alloy presented in Figure 5a mostly displays basal grains with coarser grain sizes, while the AZ61-0.5CaO and AZ61-1CaO alloys display some non-basal grains with finer grain sizes (Figure 5d,g). The KAM maps of the heat-treated alloys shown in Figure 5b,e,h exhibit lower KAM values compared to those of the non-annealed alloys. This reduction is attributed to the strain-free grains formed by recrystallization during the heat treatment. It also shows that there is no change in KAM values from AZ61 alloys to AZ61-0.5CaO alloys, whereas the KAM value of AZ61-1CaO shows a notable reduction.

Furthermore, the basal pole figure illustrated in Figure 5c,f,i shows the influence of CaO addition on the textural evolution of AZ61 alloys during hot rolling and subsequent heat treatment. In AZ61 alloys, a strong basal texture is observed, with a maximum intensity of 17.4 m.r.d. (Figure 5c). The addition of CaO led to the splitting of basal poles toward RD and a decrease in the maximum intensity to 13.7 m.r.d. for AZ61-0.5CaO alloys (Figure 5f). In the case of AZ61-1CaO alloys, there is spreading of basal poles perpendicular to the normal direction as shown in Figure 5i. Overall, the addition of CaO to AZ61 alloys leads to the splitting and spreading of basal poles away from the normal direction, which suggests the evolution of non-basal poles and basal texture weakening.

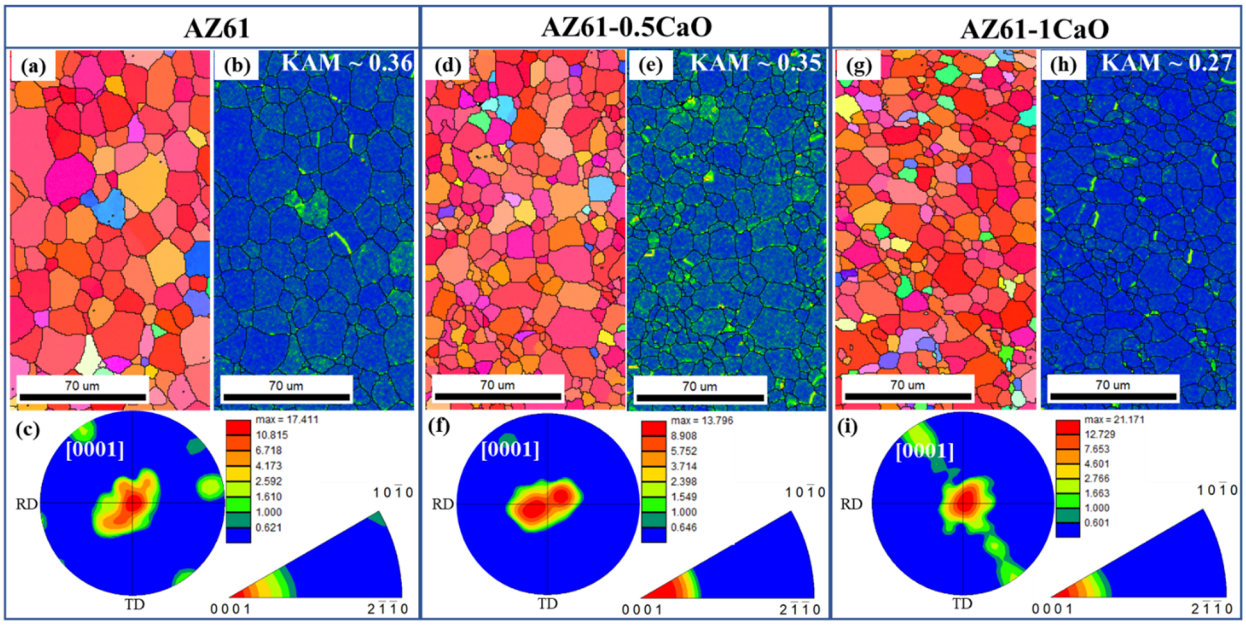


Figure 5. EBSD analysis including the (**a**,**d**,**g**) inverse pole figure map, (**b**,**e**,**h**) Kernel average misorientation map and (**c**,**f**,**i**) (0001) pole figure for annealed AZ61, AZ61-0.5Ca and AZ61-1CaO.

Further microstructural analysis of the heat-treated alloys was conducted using grain size distribution and misorientation distribution maps, as depicted in Figure 6. The average grain size of AZ61 alloys was 13.25 µm, which was higher as compared to both AZ61-0.5CaO (8.88 µm) and AZ61-1CaO (8.6 µm) as presented in Figure 6a–c. The grain size distribution also reveals that AZ61 alloys exhibit a wide range of grain sizes from 3.4 to 35 µm, while AZ61-0.5CaO and AZ61-1Ca0 show a narrower range from 3.2 to 25.5 µm. This indicates that the addition of CaO to AZ61 alloys has resulted in the development of finer and more uniformly sized grains. The primary factor for the evolution of finer grains in AZ61-0.5CaO and AZ61-1CaO is the existence of second-phase particles, resulting in a particle-stimulated nucleation (PSN) recrystallization during hot rolling and subsequent heat treatment. It is worth noticing that the sizes of second-phase particles in the present study are higher than the previously reported critical size (0.1 µm) to initiate PSN recrystallization.

The misorientation angle distribution presented in Figure 6d–f demonstrated that the addition of CaO to AZ61 alloys resulted in a substantial reduction in the fraction of LAGBs (misorientations less than 15°) and an increase in the fraction of HAGBs (misorientations greater than 15°). No significant fraction near the misorientation angle of 86° indicates the absence of twins in all the heat-treated alloys. Therefore, the main reason for the higher HAGBs in CaO-containing alloys after heat treatment is the presence of finer grains.

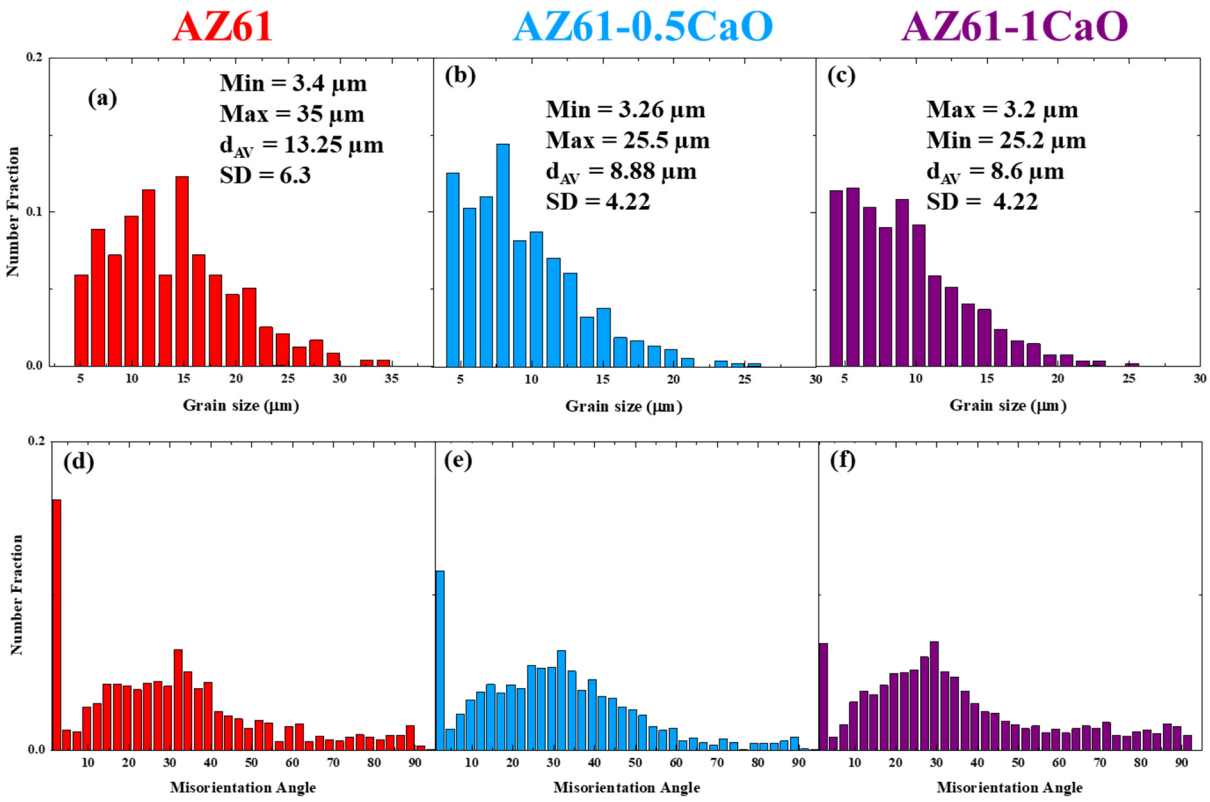


Figure 6. Grain size distribution and misorientation angle distribution of the annealed AZ61 (**a**,**d**), AZ61-0.5Ca (**b**,**e**) and AZ61-1CaO (**c**,**f**).

To elucidate the influence of annealing treatment on the mechanical performance of AZ61 and AZ61-xCaO, room-temperature tensile tests were carried out at the strain rate of 0.001 s^{-1}. Figure 7 represents the characteristic true stress–strain curve of the non-annealed and annealed samples, and the yield strength (YS), ultimate tensile strength (UTS) and elongation are summarized in Table 1. It can be seen from Figure 7a that the elongation is slightly reduced with the increase in CaO in AZ61 and the elongation was observed to be 0.22, 0.21 and 0.17 for AZ61, AZ61-0.5CaO and AZ61-1CaO, respectively. The decrease in elongation can be associated with the higher twinning propensity nucleated during the primary rolling process as confirmed by the IPF presented in Figure 3. The higher fraction of twins can lead to multiple twin–twin interactions and act as an obstacle to the dislocation moment [58,59]. As a result, the stress is concentrated in the local areas leading to crack nucleation due to the higher stress concentration, which is confirmed by the KAM maps shown in Figure 3b,e,h. For annealed samples (Figure 7b), AZ61 displayed a small reduction in mechanical performance, while AZ61-1CaO showed the highest YS (203 MPa) and UTS (330 MPa), and elongation was also significantly increased as compared to the non-annealed counterpart. AZ61-0.5CaO in the annealed condition also displayed an increase in elongation as compared to the non-annealed condition. The exceptional increase in the YS and UTS of AZ61-1CaO can be attributed to the presence of discernable precipitates as presented in SEM images in Figure 2, which strengthened the alloy via precipitation strengthening.

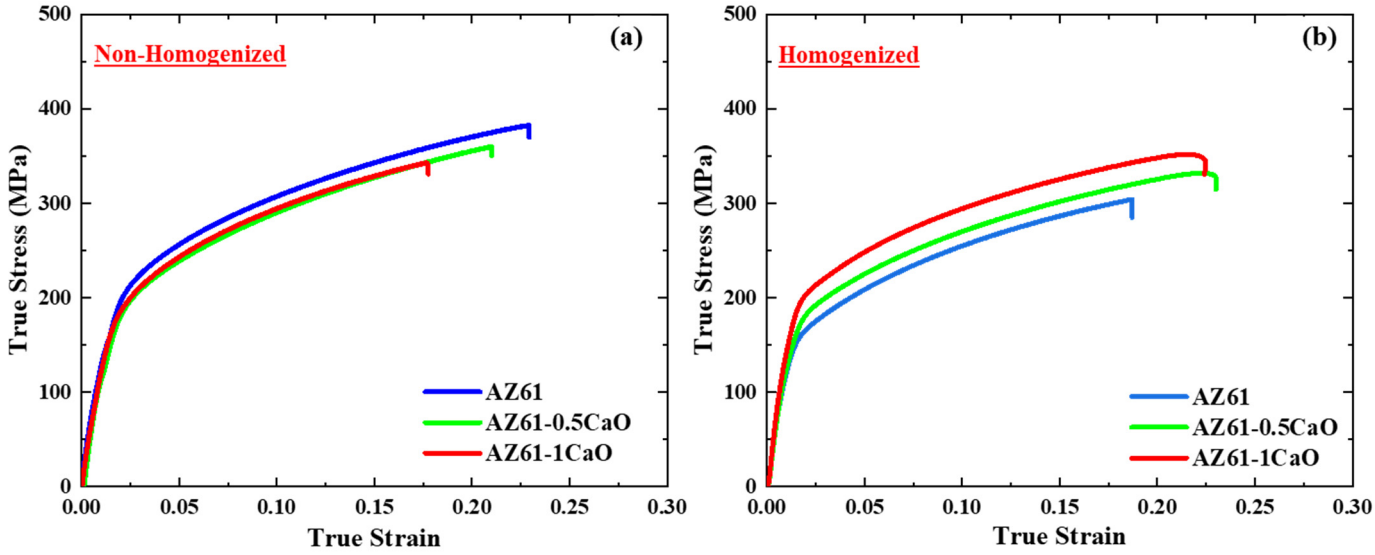


Figure 7. Representative true stress–strain curve of AZ61, AZ61-0.5CaO and AZ61-1CaO in the (**a**) non-annealed and (**b**) annealed conditions.

Table 1. Mechanical properties of annealed and non-annealed AZ61, AZ61-0.5CaO and AZ61-1CaO.

Condition	Material	YS (MPa)	UTS (MPa)	True Strain
As-fabricated	AZ61	195 ± 1.1	382 ± 1.5	0.22
	AZ61-0.5CaO	180 ± 2.1	350 ± 2.6	0.21
	AZ61-1CaO	184 ± 1.6	331 ± 2.2	0.17
Annealed	AZ61	166 ± 1.4	304 ± 2.7	0.18
	AZ61-0.5CaO	181 ± 1.7	324 ± 2.1	0.23
	AZ61-1CaO	203 ± 3.5	330 ± 3.8	0.22

4. Conclusions

In the present study, the effect of annealing treatment on the room-temperature mechanical performance of AZ61, AZ61-0.5CaO and AZ61-1CaO was thoroughly investigated. Samples showed a significantly higher fraction of tension twinning due to the primary rolling process, and the twinning propensity was increased by the addition of CaO. The SEM-EDS analysis showed the formation of intermetallic precipitates and TEM confirmed the precipitates to be $(Mg, Al)_2Ca$. The detailed EBSD analysis revealed an intricate twinned structure in all the samples and the highest $\{10\bar{1}2\}$ tension twinning fraction was recorded for AZ61-1CaO (21%), which was consistent with the (0002) pole figure. The EBSD-based KAM maps showed the highest stress accumulation near the grain boundaries and the highest value was obtained for AZ61-0.5CaO (0.72°). The high stored strain energy in the non-annealed samples was attributed to the complex twinned structure and dispersed precipitates, which can impede the dislocation moment, resulting in strain accumulation. Furthermore, the annealing treatment resulted in the grain growth and removal of {10–12} tension twins, which reduced the stored strain energy in the microstructure. The room-temperature tensile tests revealed that the mechanical properties of AZ61 were reduced by the addition of CaO, which was attributed to the higher local stress concentration due to twin–twin interactions. Moreover, the annealing treatment led to significant enhancement in the YS and UTS of AZ61-1CaO, which is related to the precipitation hardening induced by the intermetallic precipitates.

Author Contributions: Conceptualization, U.M.C. and T.-S.J.; Methodology, U.M.C., H.M.R.T., N.A. and A.M.; Formal analysis, U.M.C., H.M.R.T. and N.A.; Investigation, A.M. and K.H.; Resources, M.K.K. and K.H.; Data curation, N.A. and A.M.; Writing—original draft, U.M.C. and N.A.; Writing—review and editing, T.-S.J.; Supervision, M.K.K. and T.-S.J.; Project administration, K.H. and T.-S.J.; Funding acquisition, T.-S.J. All authors have read and agreed to the published version of the manuscript.

Funding: This work was supported by the National Research Foundation of Korea (NRF) grant funded by the Korean government (MSIT) (No. 2020R1C1C1004434) and Post-Doctoral Research Program for Excellence Institute (2022) in the Incheon National University.

Data Availability Statement: Data are contained within the article.

Conflicts of Interest: The authors declare no conflict of interest.

References

1. Masood Chaudry, U.; Hamad, K.; Kim, J.-G. A further improvement in the room-temperature formability of magnesium alloy sheets by pre-stretching. *Materials* **2020**, *13*, 2633. [CrossRef] [PubMed]
2. Atrens, A.; Song, G.L.; Liu, M.; Shi, Z.; Cao, F.; Dargusch, M.S. Review of recent developments in the field of magnesium corrosion. *Adv. Eng. Mater.* **2015**, *17*, 400–453. [CrossRef]
3. Song, B.; Guo, N.; Liu, T.; Yang, Q. Improvement of formability and mechanical properties of magnesium alloys via pre-twinning: A review. *Mater. Des.* **2014**, *62*, 352–360. [CrossRef]
4. Malik, A.; Wang, Y.; Huanwu, C.; Nazeer, F.; Khan, M.A. What is the major problem with wrought Mg alloys? *Results Engineering* **2020**, *7*, 100162. [CrossRef]
5. Malik, A.; Wang, Y.; Huanwu, C.; Bhatti, T.M.; Nazeer, F. Superplastic behavior of fine-grained extruded ZK61 Mg alloy. *Results Phys.* **2021**, *20*, 103731. [CrossRef]
6. Malik, A.; Wang, Y.; Cheng, H.; Nazeer, F.; Khan, M.A. Microstructure evolution of Mg-Zn-Zr magnesium alloy against soft steel core projectile. *J. Mater. Sci. Technol.* **2021**, *79*, 46–61. [CrossRef]
7. Guan, D.; Rainforth, W.M.; Ma, L.; Wynne, B.; Gao, J. Twin recrystallization mechanisms and exceptional contribution to texture evolution during annealing in a magnesium alloy. *Acta Mater.* **2017**, *126*, 132–144. [CrossRef]
8. Hadorn, J.P.; Mulay, R.P.; Hantzsche, K.; Yi, S.; Bohlen, J.; Letzig, D.; Agnew, S.R. Texture Weakening Effects in Ce-Containing Mg Alloys. *Met. Mater. Trans. A* **2013**, *44*, 1566–1576. [CrossRef]
9. Jia, W.; Hu, X.; Zhao, H.; Ju, D.; Chen, D. Texture evolution of AZ31 magnesium alloy sheets during warm rolling. *J. Alloys Compd.* **2015**, *645*, 70–77. [CrossRef]
10. Chaudry, U.M.; Hamad, K.; Jun, T.-S. Investigating the Microstructure, Crystallographic Texture and Mechanical Behavior of Hot-Rolled Pure Mg and Mg-2Al-1Zn-1Ca Alloy. *Crystals* **2022**, *12*, 1330. [CrossRef]
11. Park, S.H.; Lee, J.H.; Huh, Y.-H.; Hong, S.-G. Enhancing the effect of texture control using {1 0− 1 2} twins by retarding detwinning activity in rolled Mg–3Al–1Zn alloy. *Scr. Mater.* **2013**, *69*, 797–800. [CrossRef]
12. Agnew, S.; Horton, J.; Lillo, T.; Brown, D. Enhanced ductility in strongly textured magnesium produced by equal channel angular processing. *Scr. Mater.* **2004**, *50*, 377–381. [CrossRef]
13. Ansari, N.; Lee, S.Y.; Singh, S.S.; Jain, J. Effect of rolling routes on the microstructure, texture and mechanical properties of Mg-5Y binary alloy. *Philos. Mag.* **2023**, *103*, 840–859. [CrossRef]
14. Wu, Z.; Curtin, W. The origins of high hardening and low ductility in magnesium. *Nature* **2015**, *526*, 62–67. [CrossRef]
15. Barnett, M.R.; Nave, M.D.; Bettles, C.J. Deformation microstructures and textures of some cold rolled Mg alloys. *Mater. Sci. Eng. A* **2004**, *386*, 205–211. [CrossRef]
16. Stanford, N.; Barnett, M. Effect of composition on the texture and deformation behaviour of wrought Mg alloys. *Scr. Mater.* **2008**, *58*, 179–182. [CrossRef]
17. Watanabe, H.; Mukai, T.; Ishikawa, K. Effect of temperature of differential speed rolling on room temperature mechanical properties and texture in an AZ31 magnesium alloy. *J. Mater. Process. Technol.* **2007**, *182*, 644–647. [CrossRef]
18. Wang, L.; Mostaed, E.; Cao, X.; Huang, G.; Fabrizi, A.; Bonollo, F.; Chi, C.; Vedani, M. Effects of texture and grain size on mechanical properties of AZ80 magnesium alloys at lower temperatures. *Mater. Des.* **2016**, *89*, 1–8. [CrossRef]
19. Lee, H.-J.; Lee, S.K.; Jung, K.H.; Lee, G.A.; Ahn, B.; Kawasaki, M.; Langdon, T.G. Evolution in hardness and texture of a ZK60A magnesium alloy processed by high-pressure torsion. *Mater. Sci. Eng. A* **2015**, *630*, 90–98. [CrossRef]
20. Ali, S.; Karunanithi, R.; Prashanth, M.; Rahman, M.A. X-ray peak broadening on microstructure, and structural properties of titanium and Ti-6Al-4V alloys. *Mater. Today Proc.* **2020**, *27*, 2390–2393. [CrossRef]
21. Dobatkin, S.; Rokhlin, L.; Lukyanova, E.; Murashkin, M.Y.; Dobatkina, T.; Tabachkova, N.Y. Structure and mechanical properties of the Mg-Y-Gd-Zr alloy after high pressure torsion. *Mater. Sci. Eng. A* **2016**, *667*, 217–223. [CrossRef]
22. Lukyanova, E.A.; Martynenko, N.S.; Serebryany, V.N.; Belyakov, A.N.; Rokhlin, L.L.; Dobatkin, S.V.; Estrin, Y.Z. Structure and mechanical and corrosion properties of a magnesium Mg–Y–Nd–Zr alloy after high pressure torsion. *Russ. Metall.* **2017**, *2017*, 912–921. [CrossRef]

23. Zhao, C.; Li, Z.; Shi, J.; Chen, X.; Tu, T.; Luo, Z.; Cheng, R.; Atrens, A.; Pan, F. Strain hardening behavior of Mg–Y alloys after extrusion process. *J. Magnes. Alloys* **2019**, *7*, 672–680. [CrossRef]
24. Zhang, L.; Wu, X.; Yang, X.; Li, Y. Static recrystallization and precipitation behavior of forged and annealed Mg–8.7 Gd–4.18 Y–0.42 Zr magnesium alloy. *Mater. Today Commun.* **2023**, *34*, 105106. [CrossRef]
25. Mackenzie, L.; Pekguleryuz, M. The recrystallization and texture of magnesium–zinc–cerium alloys. *Scr. Mater.* **2008**, *59*, 665–668. [CrossRef]
26. Yu, Z.; Xu, X.; Mansoor, A.; Du, B.; Shi, K.; Liu, K.; Li, S.; Du, W. Precipitate characteristics and their effects on the mechanical properties of as-extruded Mg-Gd-Li-Y-Zn alloy. *J. Mater. Sci. Technol.* **2021**, *88*, 21–35. [CrossRef]
27. Yu, Z.; Liu, L.; Mansoor, A.; Liu, K.; Li, S.; Du, W. Microstructures and mechanical properties of as-extruded Mg–8Gd–2Y–1Zn–6Li alloy. *J. Alloys Compd.* **2021**, *864*, 158826. [CrossRef]
28. Mansoor, A.; Du, W.; Yu, Z.; Ding, N.; Fu, J.; Jia, L.; Liu, K.; Li, S. Effect of Secondary Extrusion on the Microstructure and Mechanical Properties of Mg-12Gd-2Er-0.4 Zr Alloy. *J. Mater. Eng. Perform.* **2021**, *30*, 8996–9007. [CrossRef]
29. Kocich, R.; Kunčická, L.; Král, P.; Lowe, T.C. Texture, deformation twinning and hardening in a newly developed Mg–Dy–Al–Zn–Zr alloy processed with high pressure torsion. *Mater. Des.* **2016**, *90*, 1092–1099. [CrossRef]
30. Chaudry, U.M.; Noh, Y.; Han, G.; Jaafreh, R.; Jun, T.-S.; Hamad, K. Effect of CaO on structure and properties of AZ61 magnesium alloy. *Mater. Sci. Eng. A* **2022**, *844*, 143189. [CrossRef]
31. Bhattacharyya, J.J.; Agnew, S.; Muralidharan, G. Texture enhancement during grain growth of magnesium alloy AZ31B. *Acta Mater.* **2015**, *86*, 80–94. [CrossRef]
32. Kim, S.-H.; You, B.-S.; Yim, C.D.; Seo, Y.-M. Texture and microstructure changes in asymmetrically hot rolled AZ31 magnesium alloy sheets. *Mater. Lett.* **2005**, *59*, 3876–3880. [CrossRef]
33. Kim, H.; Lee, J.-H.; Lee, C.; Bang, W.; Ahn, S.; Chang, Y. Shear band formation during hot compression of AZ31 Mg alloy sheets. *Mater. Sci. Eng. A* **2012**, *558*, 431–438. [CrossRef]
34. Pei, R.; Zou, Y.; Zubair, M.; Wei, D.; Al-Samman, T. Synergistic effect of Y and Ca addition on the texture modification in AZ31B magnesium alloy. *Acta Mater.* **2022**, *233*, 117990. [CrossRef]
35. Lee, J.U.; Kim, Y.J.; Park, S.H. Microstructure evolution maps of AZ31 and AZ91–Ca–Y–MM alloys under precompression and subsequent annealing conditions. *Mater. Sci. Eng. A* **2022**, *854*, 143814. [CrossRef]
36. Li, X.; Yang, P.; Wang, L.-N.; Meng, L.; Cui, F.-E. Orientational analysis of static recrystallization at compression twins in a magnesium alloy AZ31. *Mater. Sci. Eng. A* **2009**, *517*, 160–169. [CrossRef]
37. Agnew, S. Plastic anisotropy of magnesium alloy AZ31B sheet. In *Essential Readings in Magnesium Technology*; Springer: Berlin/Heidelberg, Germany, 2016; pp. 351–356.
38. Hu, L.; Lv, H.; Shi, L.; Chen, Y.; Chen, Q.; Zhou, T.; Li, M.; Yang, M. Research on deformation mechanism of AZ31 magnesium alloy sheet with non-basal texture during uniaxial tension at room temperature: A visco-plastic self-consistent analysis. *J. Magnes. Alloys* **2022**, *10*, 1994–2008. [CrossRef]
39. He, S.M.; Zeng, X.Q.; Peng, L.M.; Gao X-q Nie, J.F.; Ding, W.J. Precipitation in a Mg–10Gd–3Y–0.4 Zr (wt.%) alloy during isothermal ageing at 250 C. *J. Alloys Compd.* **2006**, *421*, 309–313. [CrossRef]
40. Bourezg, Y.I.; Azzeddine, H.; Baudin, T.; Helbert, A.-L.; Huang, Y.; Bradai, D.; Langdon, T.G. Texture and microhardness of Mg-Rare Earth (Nd and Ce) alloys processed by high-pressure torsion. *Mater. Sci. Eng. A* **2018**, *724*, 477–485. [CrossRef]
41. Wu, B.; Zhao, Y.; Du, X.; Zhang, Y.; Wagner, F.; Esling, C. Ductility enhancement of extruded magnesium via yttrium addition. *Mater. Sci. Eng. A* **2010**, *527*, 4334–4340. [CrossRef]
42. Pei, Z.; Li, R. The effect of yttrium on the generalized stacking fault energies in Mg. *Comput. Mater. Sci.* **2017**, *133*, 1–5. [CrossRef]
43. Kim, K.-H.; Jeon, J.B.; Kim, N.J.; Lee, B.-J. Role of yttrium in activation of< c+ a> slip in magnesium: An atomistic approach. *Scr. Mater.* **2015**, *108*, 104–108.
44. Chaudry, U.M.; Noh, Y.; Hamad, K.; Jun, T.-S. Effect of deformation temperature on the slip activity in pure Mg and AZX211. *J. Mater. Res. Technol.* **2022**, *19*, 3406–3420. [CrossRef]
45. Ha, C.; Bohlen, J.; Zhou, X.; Brokmeier, H.-G.; Kainer, K.; Schell, N.; Letzig, D.; Yi, S. Texture development and dislocation activities in Mg-Nd and Mg-Ca alloy sheets. *Mater. Charact.* **2021**, *175*, 111044. [CrossRef]
46. Guo, F.; Jiang, L.; Yang, M.; Ma, Y.; Deng, Y.; Zhang, D.; Pan, F. Tailoring the rolling texture of AZ31 Mg Alloy with Calcium and Tin Addition. *Adv. Eng. Mater.* **2019**, *21*, 1800920. [CrossRef]
47. Fu, J.; Du, W.; Liu, K.; Du, X.; Zhao, C.; Liang, H.; Mansoor, A.; Li, S.; Wang, Z. Effect of the Ca2Mg6Zn3 Phase on the Corrosion Behavior of Biodegradable Mg-4.0 Zn-0.2 Mn-x Ca Alloys in Hank's Solution. *Materials* **2022**, *15*, 2079. [CrossRef]
48. Liu, B.-Y.; Liu, F.; Yang, N.; Zhai, X.-B.; Zhang, L.; Yang, Y.; Li, B.; Li, J.; Ma, E.; Nie, J.-F.; et al. Large plasticity in magnesium mediated by pyramidal dislocations. *Science* **2019**, *365*, 73–75. [CrossRef]
49. Razavi, S.; Foley, D.; Karaman, I.; Hartwig, K.; Duygulu, O.; Kecskes, L.; Mathaudhu, S.N.; Hammond, V.H. Effect of grain size on prismatic slip in Mg–3Al–1Zn alloy. *Scr. Mater.* **2012**, *67*, 439–442. [CrossRef]
50. Akhtar, A.; Teghtsoonian, E. Solid solution strengthening of magnesium single crystals—ii the effect of solute on the ease of prismatic slip. *Acta Metall.* **1969**, *17*, 1351–1356. [CrossRef]
51. Zhao, J.; You, C.; Chen, M.; Lyu, S.; Tie, D.; Liu, H. Effect of calcium oxide particle size on microstructure and properties of AZ91 Mg alloy. *J. Alloys Compd.* **2021**, *886*, 160970. [CrossRef]

52. Lee, T.W.; Park, H.W.; Lim, H.; Kim, S.K.; Lim, S.H. Microstructural characterization of oxide layers in CaO added AZ31 Mg alloy. *J. Alloys Compd.* **2017**, *714*, 397–408. [CrossRef]
53. Liu, Y.H.; Li, X.G.; Li, Y.J.; Shi, G.L.; Yuan, J.W.; Zhang, K. Homogenization treatment of Mg-6Zn-3Sn (wt.%) alloy and its effects on microstructure and mechanical properties. *Trans. Nonferrous Met. Soc. China* **2023**, *33*, 67–78. [CrossRef]
54. Chaudry, U.M.; Tariq, H.M.R.; Ansari, N.; Kim, C.-S.; Lee, S.Y.; Jun, T.-S. Exceptional improvement in the yield strength of AZ61 magnesium alloy via cryo-stretching and its implications on the grain growth during annealing. *J. Alloys Compd.* **2024**, *970*, 172630. [CrossRef]
55. Jeong, J.; Im, J.; Song, K.; Kwon, M.; Kim, S.K.; Kang, Y.B.; Oh, S.H. Transmission electron microscopy and thermodynamic studies of CaO-added AZ31 Mg alloys. *Acta Mater.* **2013**, *61*, 3267–3277. [CrossRef]
56. Amberger, D.; Eisenlohr, P.; Göken, M. On the importance of a connected hard-phase skeleton for the creep resistance of Mg alloys. *Acta Mater.* **2012**, *60*, 2277–2289. [CrossRef]
57. Park, J.; Kim, M.; Yoon, U.; Kim, W. Microstructures and mechanical properties of Mg–Al–Zn–Ca alloys fabricated by high frequency electromagnetic casting method. *J. Mater. Sci.* **2009**, *44*, 47–54. [CrossRef]
58. Chaudry, U.M.; Tariq, H.M.R.; Zubair, M.; Ansari, N.; Jun, T.-S. Implications of twinning on the microstructure development, crystallographic texture and mechanical performance of Mg alloys-a critical review. *J. Magnes. Alloys* **2023**, in press. [CrossRef]
59. Zhang, K.; Shao, Z.; Daniel, C.S.; Turski, M.; Pruncu, C.; Lang, L.; Robson, J.; Jiang, J. A comparative study of plastic deformation mechanisms in room-temperature and cryogenically deformed magnesium alloy AZ31. *Mater. Sci. Eng. A* **2021**, *807*, 140821. [CrossRef]

Disclaimer/Publisher's Note: The statements, opinions and data contained in all publications are solely those of the individual author(s) and contributor(s) and not of MDPI and/or the editor(s). MDPI and/or the editor(s) disclaim responsibility for any injury to people or property resulting from any ideas, methods, instructions or products referred to in the content.